Role of disorder and correlations in the metal-insulator transition in ultrathin $SrVO_3$ films

Gaomin Wang,[1] Zhen Wang,[1,2] Meng Meng,[1] Mohammad Saghayezhian,[1] Lina Chen,[1] Chen Chen,[1] Hangwen Guo,[1] Yimei Zhu,[2] E. W. Plummer,[1] and Jiandi Zhang[1,*]

[1]*Department of Physics and Astronomy, Louisiana State University, Baton Rouge, Louisiana 70803, USA*

[2]*Brookhaven National Laboratory, Upton, New York 11973, USA*

(Received 29 March 2019; revised manuscript received 29 July 2019; published 7 October 2019)

Metallic oxide $SrVO_3$ represents a prototype system for the study of the mechanism behind thickness-induced metal-to-insulator transition (MIT) or crossover in thin films due to its simple cubic symmetry with one electron in the $3d$ state in the bulk. Here we report a deviation of chemical composition and distortion of lattice structure existing in the initial 3 unit cells of $SrVO_3$ films grown on $SrTiO_3$ (001) from its bulk form, which shows a direct correlation to the thickness-dependent MIT. *In situ* photoemission and scanning tunneling spectroscopy indicate a MIT at the critical thickness of ∼3 unit cells (u.c.), which coincides with the formation of a $(\sqrt{2} \times \sqrt{2})$ $R45^\circ$ surface reconstruction. However, atomically resolved scanning transmission electron microscopy and electron energy loss spectroscopy show depletion of Sr, and a change of V valence, thus implying the existence of a significant amount of oxygen vacancies in the 3 u.c. of $SrVO_3$ near the interface. Transport and magnetotransport measurements further reveal that disorder, rather than electron correlations, is likely to be the main cause for the MIT in the $SrVO_3$ ultrathin films.

DOI: 10.1103/PhysRevB.100.155114

I. INTRODUCTION

Transition metal oxides have been one of the most-studied systems in condensed matter research for many decades. The strong coupling between charge, spin, and lattice in these strongly correlated systems gives rise to a variety of fantastic phenomena such as high-temperature superconductivity [1], colossal magnetoresistance [2], and multiferroicity [3]. Among the family of transition metal oxides, $SrVO_3$ (SVO) is a promising material that has recently attracted much attention for proposed applications as conducting electrodes [4] and transparent conductors [5]. Being a highly correlated paramagnetic metallic oxide, SVO is known to undergo metal-insulator transition (MIT) upon doping or reduced dimensionality such as in thin film form [6,7]. The simple cubic structure and absence of magnetic ordering in SVO makes it a prototype for the study of the mechanism behind metal-insulator transition, like structure distortion, electron correlations, and disorder-induced localization.

Angle-resolved photoemission spectroscopy (ARPES) study reported that MIT occurs at a critical thickness of 2–3 unit cells for SVO thin films grown on a $SrTiO_3$ (001) (STO) substrate [6]. Based on Mott-Hubbard theory, MIT can be controlled by tuning the magnitudes of the on-site Coulomb repulsion U and bandwidth W [8,9]. Going from bulk to thin films, the decrease in film thickness results in a reduction in the effective coordination number of constituent ions at the interface and surface, therefore reducing the effective bandwidth W which may drive the system into MIT [6]. However, the change of lattice structure and/or chemical composition near the interface/surface may drastically alter the film properties in the ultrathin limit. Recent studies with scanning tunneling microscopy (STM) and spectroscopy (STS) [10,11] reported that the surface of SVO has two distinct surface terminations associated with two surface reconstructions, a $(\sqrt{2} \times \sqrt{2})$ $R45^\circ$ and $(\sqrt{2} \times \sqrt{2})$ $R26.5^\circ$, respectively. These reconstructions may be an important factor to influence metallicity, hence the observed MIT. While the role of surface reconstruction in MIT has been studied, the effect of structure and stoichiometry on MIT is neither well studied nor understood. Furthermore, the disorder caused by defects such as oxygen vacancies and interface intermixing is almost unavoidable near the interface. Scanning transmission electron microscopy (STEM) study [12] on $SrVO_3/LaAlO_3$ (SVO/LAO) demonstrated interfacial diffusion at the interface and that interfacial defects induce a significant change in electronic properties by showing an electronic transformation from the insulating state to metallic state at SVO/LAO heterointerfaces due to the hybridization of interfacial O $2p$ and V $3d$ orbitals. It is proposed by the scaling theory of localization that in a two-dimensional (2D) system, the existence of disorder alone will drive the system towards insulating behavior [13,14]; therefore disorder can play a crucial role in MIT. In the case of oxide thin films, disorder mostly exists in the form of oxygen vacancies, which can be easily introduced into the system during film growth at a low oxygen partial pressure or in vacuum. In addition, the presence of epitaxial strain can promote the presence of the oxygen vacancies [15]. Therefore, in order to understand the origin of MIT, the role of disorder (cation or anion) must be considered on the same grounds as electron-electron correlations. In this study, we seek to understand the role played by disorder behind the MIT in the SVO system, by investigating the structure and electronic properties of the SVO thin films with various tools including ultraviolet photoemission spectroscopy (UPS), STS, scanning

*jiandiz@lsu.edu

transmission electron microscopy (STEM), and electron energy loss spectroscopy (EELS). Our study confirms that near the SVO/STO interface where the film is under maximum strain, there indeed exist a significant amount of cation and anion defects. Moreover, by introducing more oxygen vacancies into the original metallic SVO thin films, one can eventually drive the films to insulating. We therefore conclude that disorder plays a significant role in the thickness-induced MIT.

II. EXPERIMENTAL DETAILS

The substrates used in this study were 0.1% Nb:$SrTiO_3$ (001) samples supplied by CrysTec GmbH. Before being transferred to the vacuum chamber, every substrate was cleaned with acetone, alcohol, and de-ionized water, etched with buffered HF for 30 s, and subsequently annealed at 950 °C for 1 h in oxygen to prepare an atomically flat TiO_2-terminated surface for optimized film growth. The SVO films were grown at a substrate temperature of 600 °C under a vacuum level of 1×10^{-8} Torr with laser energy of ~ 2.5 J/cm^2 and monitored by reflection high-energy electron diffraction (RHEED) to guarantee a layer-by-layer 2D growth. A stoichiometric SVO target was used for the deposition. After the growth, the films were transferred to a characterization chamber through vacuum to perform *in situ* analysis. Scanning tunneling microscopy/spectroscopy (STM/STS) was performed with instruments from Omicron. Ultraviolet photoemission spectroscopy (UPS) was performed with a SPECS PHOIBOS-150 analyzer calibrated with a gold single crystal, with a monochromated Scienta VUV 5000 helium photon source. Low-energy electron diffraction from the surface of SVO films was also performed *in situ*. Cross-section TEM samples were prepared by the focused ion beam (FIB) method with Ga^+ ions followed by Ar^+ ion nanomilling. The microscopy work was performed *ex situ* on a JEOL ARM200 microscope at Brookhaven National Laboratory (BNL) equipped with two aberration correctors. The atomic-resolved STEM images were collected with a 21-mrad convergent angle and a collection angle of 67 – 375 mrad for high-angle annular dark field (HAADF) and 11 – 23 mrad for annular bright field (ABF) imaging. All electron energy loss spectroscopy (EELS) data were acquired at a convergence semiangle of 20 mrad and a collection semiangle of 88 mrad. An energy dispersion of 0.25 eV/channel with energy resolution of $\sim$ 0.8 eV was used for fine structure study of EELS spectra. The EELS spectra of V-$L_{2,3}$, Ti-$L_{2,3}$, O-K, and Sr-$L_{2,3}$ edges were obtained simultaneously at an energy dispersion of 1 eV/channel for composition analysis. The dual EELS mode was used in order to calibrate the energy shift in the spectra collection process. After background subtraction with a power-law function and correction by a Fourier deconvolution method for removing the multiscattering effects, the SVO and STO spectra far away from the interface were used as references to calibrate elemental concentration. Elemental concentration across the interface was obtained by fitting a series of Lorentzian peaks at each atomic column (see Supplemental Material [16], Fig. S1). The resistivity and magnetoresistance were measured by a Physical Properties Measurement System (PPMS) from Quantum Design Inc. The samples for all *ex situ* measurements were capped with amorphous STO for the protection of SVO films.

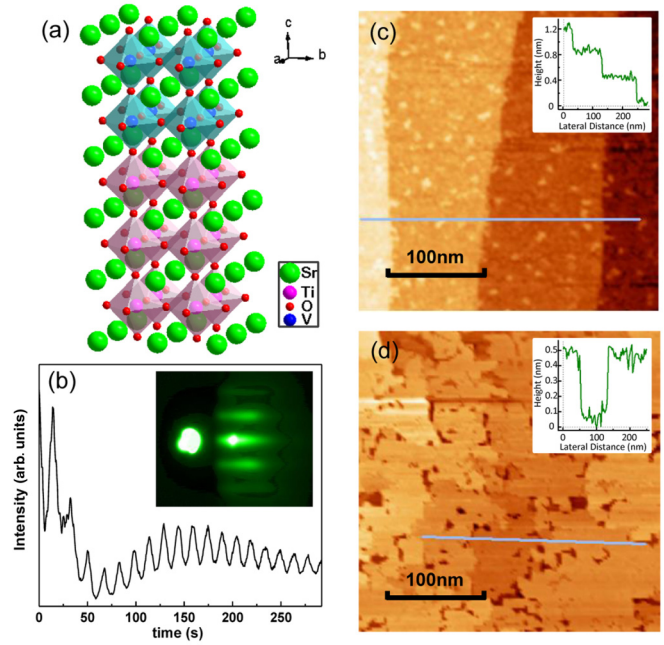

FIG. 1. (a) A structural model of $SrVO_3$ film grown on $SrTiO_3$ along the [001] direction. (b) The reflection high-energy electron diffraction (RHEED) intensity oscillation curve and pattern of a 20-u.c. $SrVO_3$ film. (c,d) The scanning tunneling microscopy (STM) images of a 3- and a 50-u.c. $SrVO_3$ film, respectively, with line profiles shown in the insets. The sizes of the images are 300 nm $\times$ 300 nm.

III. RESULTS AND DISCUSSIONS

A ball model of the SVO/STO structure is displayed in Fig. 1(a). The bulk of both SVO and STO has cubic structure, with lattice constant of 3.842 and 3.905 Å, respectively, giving the film a tensile strain with a lattice mismatch of approximately 1.6%. Figure 1(b) shows the RHEED patterns and the corresponding oscillations for a 20-u.c. SVO film, which indicates layer-by-layer 2D growth. STM morphology images and height profiles of two SVO films of thickness 3 and 50 u.c. are shown in Figs. 1(c) and 1(d). In the 3-u.c. film, a good film growth following the terraces of the STO substrate is clearly indicated; as the film grows thicker, the terrace edges are no longer distinguishable. However, the surface roughness of the 50-u.c. film is still maintained at the height of one single unit cell, as in the 3-u.c. film. The absence of small clusters on the film surface from the STM image confirms that our SVO films are fabricated in the 2D layer-by-layer fashion with atomically flat surfaces.

To confirm the thickness-dependent MIT, we have grown SVO films with different thicknesses and performed density of states measurements near Fermi energy with UPS and STS, which are shown in Fig. 2. A drop of the intensity at the Fermi edge is clearly noticeable in UPS curves of the SVO films with decreasing thickness, which eventually evolves into a gap of $\sim$0.4 eV at film thickness of 1 u.c., as shown in Fig. 2(a). The detailed intensity vs film thickness plot at the Fermi edge is

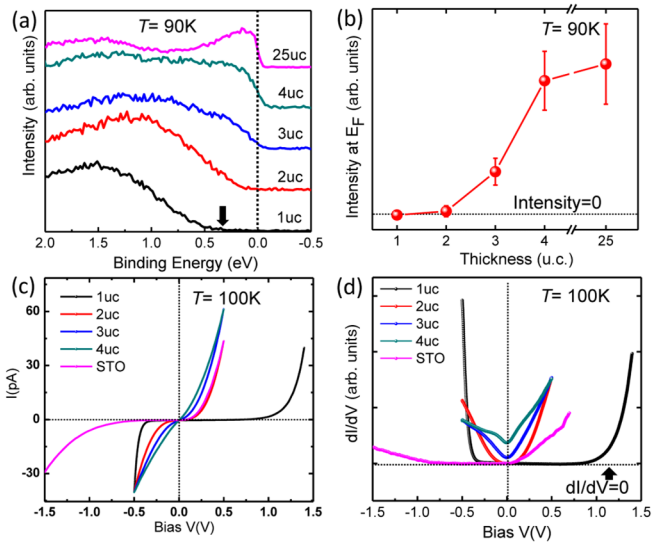

FIG. 2. (a,b) The ultraviolet photoemission spectra (UPS) of $SrVO_3$ films with thicknesses of 1–4 and 25 u.c. near the Fermi edge (E_F), and the corresponding intensity change at the Fermi edge with increasing thickness. (c) Scanning tunneling spectroscopy I-V curves for a 0.1% Nb-doped $SrTiO_3$ substrate and $SrVO_3$ films with different thicknesses. (d) dI/dV-V curves for the samples in (c), measured by the lock-in amplifier.

shown in Fig. 2(b). Given the error bar of the measurements, we can see that below 3 u.c. thickness, there is no intensity at the Fermi edge. From 3 u.c., the intensity at the Fermi edge starts to increase. The intensity at the Fermi edge for the 4-u.c. film almost reaches the same level as for the 25-u.c. one, indicating that the film becomes fully metallic, which is consistent with the results previously reported elsewhere [6].

The MIT at a critical thickness of 2–3 u.c. is also confirmed by the STS measurements. Although STS allows one to access local density states, by taking measurements on a reasonable number of points randomly sampled in different locations on the same sample, one can still compare and average the results to obtain a more general look of the film's electronic property. In our measurements of the STS current as a function of electric bias voltage (I-V) curves, ten or more points are sampled for each film, with about 20 curves taken for each point. Figure 2(c) presents the averaged I-V curves of SVO films of different thicknesses compared with the one from the STO substrate, while dI/dV as a function of electric bias voltage curves obtained by lock-in measurements of the I-V curves is displayed in Fig. 2(d). With the directly proportional relationship between dI/dV and local density of states, based on STS theory [17], dI/dV curves provide us another indication of the metallicity of the sample. From the dI/dV results, obvious gaps can be observed in the both the STO substrate and 1-u.c. SVO film; in the 2-u.c. film the gap is clearly closing and yields zero density of states only at zero bias; as the film thickness further increases, the density of states near zero bias also becomes higher, completing the MIT.

To understand the underlying mechanism of this thickness-dependent MIT, we have performed the structural characterization of SVO films with both LEED and STEM. As shown in Fig. 3(a), the LEED image appears as a $p(1 \times 1)$ pattern for the surface of a simple cubic lattice. However, fractional spots appear for the films with 3 u.c. and above as shown in Fig. 3(a) and the line profile of LEED intensity for different film thickness shown in Fig. 3(b). The LEED pattern with fractional spots indicates a $(\sqrt{2} \times \sqrt{2})R45^\circ$ surface reconstruction. Such a surface reconstruction has been observed previously by LEED and by STM image from thick SVO films [10,11]. The STM image seems to indicate that the superlattice surface structure is formed by a VO_2-terminated layer with apical oxygen adsorption. A 50% coverage of the apical oxygen sites (forming a $SrVO_{3.5}$ surface structure) has been suggested [10,11], which leads to the formation of the

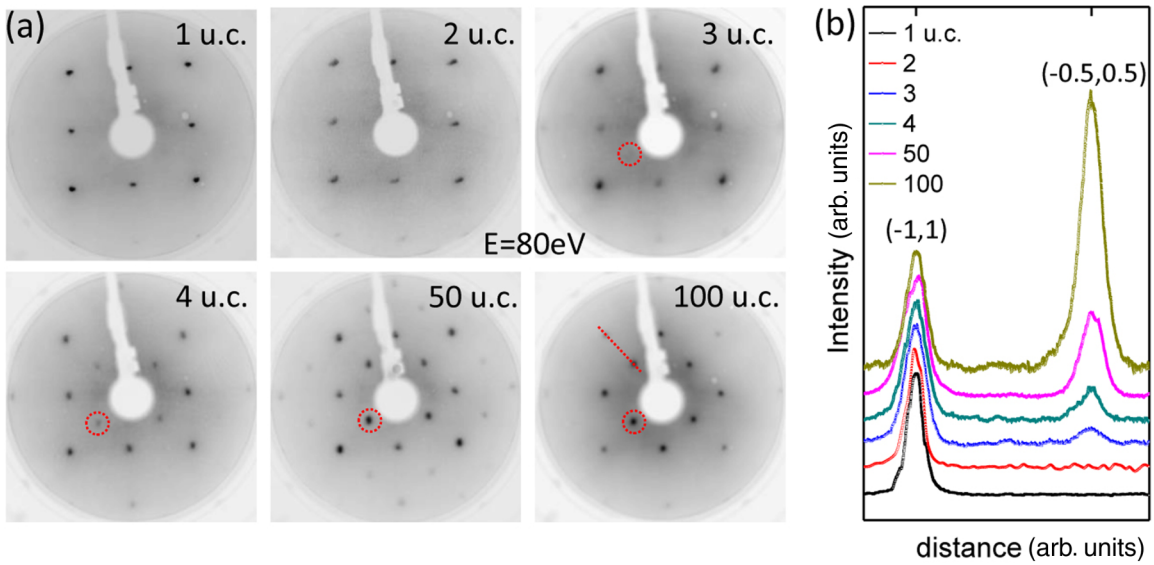

FIG. 3. Low-energy electron diffraction (LEED) patterns from the surface of $SrVO_3$ films with thicknesses of 1–4, 50, and 100 u.c. at $E = 80$ eV. (d) Intensity profiles along the cut line across the integer spot (–1,1) and the fractional spot (–0.5,0.5) from the patterns displayed in (c). The red dotted line is shown in the 100-u.c. pattern in (c) as the red dotted line. The red circles mark the fractional spots.

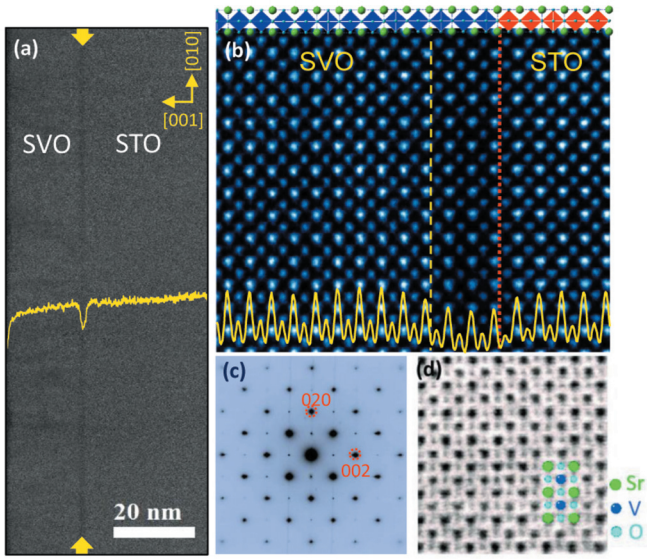

FIG. 4. (a) Low-magnification HAADF-STEM image taken along the [100] direction with intensity profile (yellow curve) across the interface of a 50-u.c. SVO film on STO(001). The arrows indicate the darker region in the SVO near the interface. (b) Enlarged HAADF-STEM image with intensity profile superimposed and ball model of the structure. The red dotted line marks the position of the interface and the yellow dotted line the SVO layers with lower intensity from the interface. (c) Selected area diffraction pattern taken along the [100] direction from the SVO film and STO substrate. (d) ABF-STEM image of the SVO film with structure model superimposed.

$(\sqrt{2} \times \sqrt{2})$ $R45^\circ$ LEED pattern. Interestingly, the formation of such ordered structure coincides with the metallization of films.

We performed STEM/EELS measurements to study atomic structure and chemical composition across the SVO/STO interface. We have chosen an SVO film with a thickness of 50 u.c. in this study to ensure the interface region is protected from degradation in the atmosphere. Figure 4(a) shows the low-magnification cross-section Z-contrast HAADF-STEM image across the SVO/STO interface taken along the [100] direction. Interestingly, there is a dark line along the interface. Figure 4(b) present an atomically resolved image near the interface. As marked by the red dotted line, the STO substrate terminates with the TiO_2 layer. The sharp interface indicates coherent epitaxial growth of the SVO film on the STO substrate. The column intensity profile curve as shown in Fig. 4(b) shows that there is a clear intensity depletion, *especially the brightness of Sr sites*, in the first 3 u.c. of the SVO films from the interface (i.e., the area from the yellow dashed line to the interface). For convenience, we will refer to the first 3 u.c. of the SVO film as the "dark area (DA)". This corresponds to the dark line near the interface observed in Fig. 4(a). The column intensity in the HAADF-STEM image is proportional with atomic number ($Z^{1.7}$) [18], and the column intensity decreases from Sr ($Z = 38$), V ($Z = 23$), to Ti ($Z = 22$). Therefore, the depletion of intensity at Sr sites in the Z-contrast HAADF-STEM image shows a deficiency of Sr in the first 3 u.c. of the SVO film. On the other hand, the SVO film has a simple cubic structure (except the DA region) as the substrate. This is also evident from the diffraction pattern shown in Fig. 4(c), taken along the [100] direction from the SVO film and STO substrate. As displayed in Fig. 4(d), the annular bright-field (ABF)–STEM image (which is sensitive to oxygen sites) shows no observable tilt distortion of VO_6 octahedra in SVO film, consistent with cubiclike structure.

However, the first 3 u.c. of the SVO film (the DA region) shows different lattice constants and chemical composition from the rest of the film. With respect to each atomic layer in the HAADF-STEM image presented in Fig. 5(a), we plotted in Fig. 5(b) the out-of-plane lattice constant as a function of distance from the interface, averaged over 15 u.c. along the [010] direction. For the SVO film beyond the DA, the measured out-of-plane lattice constant converges to the value of bulk SVO (3.84 Å; see the dotted line). However, the out-of-plane lattice constant expands to 3.97 ± 0.4 Å in DA, larger than bulk STO (3.905 Å) which is not expected in a film under tensile strain. The abnormal lattice expansion (the same for the unit cell volume) in the DA is likely related to the existence of considerable oxygen and strontium deficiency. There have already been many reports of oxygen deficiency driving the lattice expansion in complex oxides, both in bulk and in thin film [19–22].

We explored the film further by performing EELS elemental mapping to characterize the composition distribution and electronic structure across the interface with the results shown in Figs. 5(c)–5(e). Figures 5(c)–5(e) show atomic-resolved elemental mappings of Sr-$L_{2,3}$, V-$L_{2,3}$, and Ti-$L_{2,3}$ edges. The EELS composition profile can be obtained by averaging along the interface. The elemental concentration profiles are derived from the intensity profile, which is plotted on the corresponding atomic sites in the elemental maps. The STO substrate terminates with a TiO_2 layer as expected from the substrate preparation. Assuming the Ti and V levels to be 100% in STO and SVO far away from the interface, respectively, the Ti intensity drops to ~80% in the TiO_2 termination layer of the substrate, ~30% in the first VO_2 layer and ~10% in the second VO_2 layer (see the Supplemental Material [16], Fig. S1). This suggests the existence of V-Ti intermixing at B sites within the first 1–2 u.c. of the SVO film and the top layer of the substrate. An ~10% depletion of Sr concentration is also observed within the first 3 u.c. of SVO from the interface. The EELS fine structure is related to the details of the unoccupied states. The EELS spectra of the V-$L_{2,3}$ and Ti-$L_{2,3}$ edges taken across the interface are displayed in Figs. 5(g) and 5(h). The extraction of the O-K edge in SVO is complicated by the proximity of the V-$L_{2,3}$ edge. For better comparison, the EELS spectra have been normalized to the integrated intensity under the V-L edge; the spectra of Ti-L edge are normalized to the continuum interval 25eV before the onset of the oxygen K edge. A redshift of ~ 0.4 eV of the V-L_3 peak is observed within the first 3 u.c. from the interface (i.e., the DA), indicating a reduced V valence state [12]. The two spectra of the TiO_2 termination layer and the doped VO_2 layer also shift towards lower energy, implying a decreased valence state of Ti ions [23]. The details on the valence change of V and Ti are plotted in Fig. 5(f). A drop of V valence to about ~ 3.6+ within the DA is evident. The oxidation state

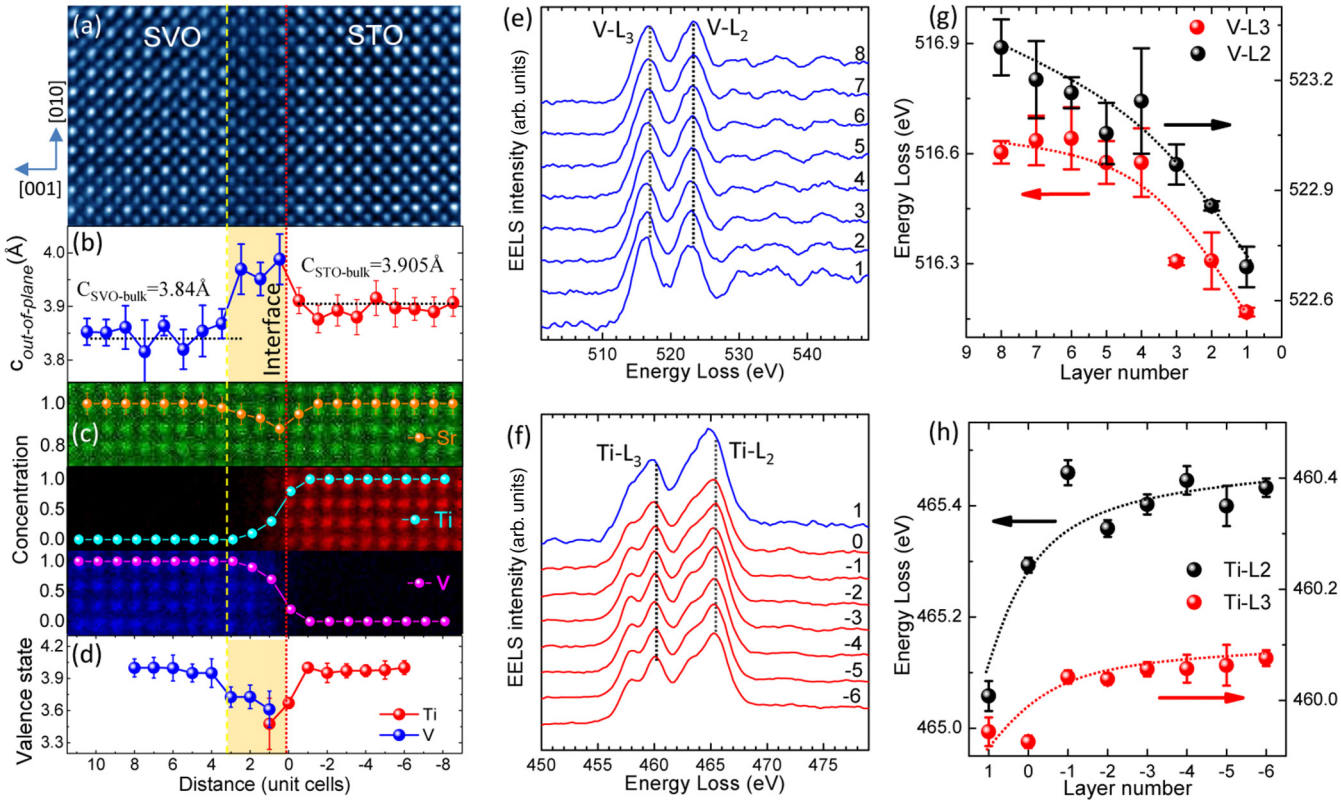

FIG. 5. (a) HAADF-STEM image across the interface between a 50-u.c. SVO film and STO substrate taken along the [100] direction. (b) Out-of-plane lattice constant as a function of distance from the interface ($x = 0$), measured from the HAADF-STEM image by averaging 20 u.c. along the [010] direction. The lattice constants for bulk STO and SVO are indicated by dotted lines. (c) False colored elemental maps for Sr (green), Ti (red), and V (blue), with lateral averaged profiles overlaid. The red dotted line marks the interface and the off-stoichiometry region of the film is highlighted. (d) Oxidation state of Ti and V ions across the interface. (e,f) Background subtracted V-$L_{2,3}$ and Ti-$L_{2,3}$ EELS spectra. (g,h) The energy of V-L and Ti-L edge peaks (the dashed lines are guide to the eyes).

of Ti decreases to $\sim 3.5+$ in the DA. As a system which does not favor tilt and rotation, and being nonpolar along the [100] direction, no polar discontinuity needs to be compensated by structural/charge reconstruction at the interface when SVO is grown on STO. In order to maintain charge neutrality near (DA) the interface, a significant amount ($\sim$10%) of oxygen deficiency is expected—one part for compensating the slight Sr deficiency, and the other part for the reduced oxidation of Ti and V. As we may recall from the previous results, the critical thickness of the metal-insulator transition for SVO films is also 3 u.c., which leads to our assumption that the oxygen deficiency may be the main driving force for the MIT.

Given the fact that the observed insulating layer thickness is 3 u.c. for the films on STO grown from different groups, and that there is a tensile strain with a lattice mismatch of approximately 1.6%, it is likely that the disorder due to O vacancies in the initial growth is related to the structural mismatch between the film and substrate, although the thermodynamic process is also important. Specifically, before film deposition, the substrate must be preheated to the growth temperature in high vacuum, such that disorder due to the O vacancies are introduced near the substrate surface in this process. However, more systematic study is needed to see the response of insulating layer thickness and disorder by varying the lattice mismatch as well as the growth condition.

As mentioned in the Introduction, disorder alone, in the form of oxygen deficiency, can drive our system into insulating. Figure 6(a) displays the sheet resistance measurements of as-grown SVO films with thicknesses from 3 to 20 u.c. The 3-u.c. film clearly shows insulating behavior, while the other films exhibit MIT or metal-insulator crossover with a sheet resistance minimum at a temperature depending on film thickness (see the marked temperature position for the minimum of each film). For a 3-u.c. film, the T dependence of resistance can be understood with the 2D variable-range hopping (VRH) model due to strong localization [24]. The 4–10-u.c. SVO films exhibit metallic behavior at high temperature, while an upturn of sheet resistance with decreasing temperature is observed in the low-temperature region, indicating the existence of weak localization. The temperature for the resistance minimum increases with decreasing film thickness, reflecting the enhancement of disorder-induced localization strength with reducing thickness, as observed in several oxide films [25–27]. In Fig. 6(b), we converted the sheet resistance to conductance and plotted the curves with respect to the logarithm of temperature. In all four films with the 4–8-u.c. films, good linear fits of sheet conductance vs $\ln T$ were obtained in the low-temperature region, which is consistent with the Anderson localization scenario though at the same time we are unable to rule out the contribution of electron-electron correlations.

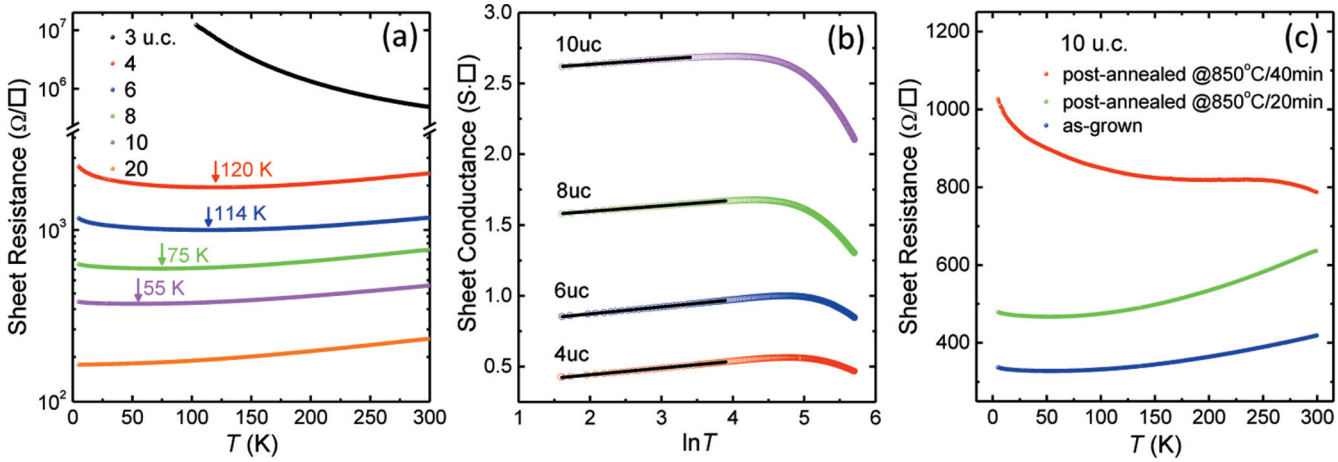

FIG. 6. (a) Resistivity vs temperature plot of $SrVO_3$ films with thicknesses of 3–20 u.c. The arrows mark the resistivity minima. (b) The conductivity of the 4–10-u.c. films, fitted to the logarithm of the temperature in the low-temperature region (5–30 K for the 10-u.c. film, and 5–50 K for the 4–8-u.c. films). (c) The resistance of a set of 10-u.c. films as grown and postannealed under 850 °C in high vacuum for different times.

If disorder due to oxygen vacancies is the origin of the insulating phase in thin SVO films, it is possible to tune a metallic SVO film to insulating by introducing more oxygen deficiency into the film on purpose. We tested our hypothesis by postannealing the SVO films in vacuum and under higher temperature than the growth temperature, so that more oxygen vacancies can be introduced to the films. Figure 6(c) presents the transport measurements for a 10-u.c. film by different vacuum-postannealing times which introduce different vacancy concentrations. The as-grown 10-u.c. film shows metallic behavior [the same as the 10-u.c. film shown in Fig. 6(a)]. When postannealed at 850 °C for 20 min, the film remained metallic, while as the annealing time increased to 40 min, the film became insulating. This shows that by introducing more oxygen deficiency, we are able to drive the original metallic SVO film to an insulating one. Such enhancement of O vacancies by annealing is also confirmed by the reduction of V valence determined by our EELS measurements on the postannealed films (see Supplemental Material [16], Fig. S2).

To further understand the nature of localization-induced insulating behavior, we have also measured the magnetoresistance (MR) for a set of SVO films, including the 10-u.c. films with and without postannealing. It has been predicted by theory that disorder-induced localization leads to negative MR [28–30] while electron-electron correlations lead to positive MR [31]. In Figs. 7(a)–7(c), we presented the MR of 4-, 6-, and 10-u.c. SVO films under different temperatures. The magnetic fields applied were normal to the film. At 5 K, the MR for the 4-u.c. film is negative, indicating the dominance of disorder-induced localization, while for the 10-u.c. film, this negative MR effect is no longer visible. Instead, positive MR emerges although the value of MR is almost 10 times smaller than that of the 4-u.c. film. However, after the vacuum-postannealing treatment that introduces more oxygen vacancies, the MR for the 10-u.c. film started to turn negative again, as shown in Fig. 7(d) and compared with Fig. 7(c). Combined with our transport results, we can conclude that disorder-induced localization is responsible for insulating behavior at low temperature for ultrathin film. Such disorder effect is amplified with reduced film thickness or vacuum postannealing, based on the enhancement of negative magnetoresistance. With increasing temperature or film thickness (see at $T = 9$ and 13 K, for example), the negative magnetoresistance drastically decreases while the weak positive magnetoresistance emerges. The positive magnetoresistance, which is likely due to the contribution of electron correlations, is not strongly dependent on the film thickness in such ultrathin film case. Therefore, the disorder effect, which is enhanced with reducing film thickness, is the major driving force behind the MIT.

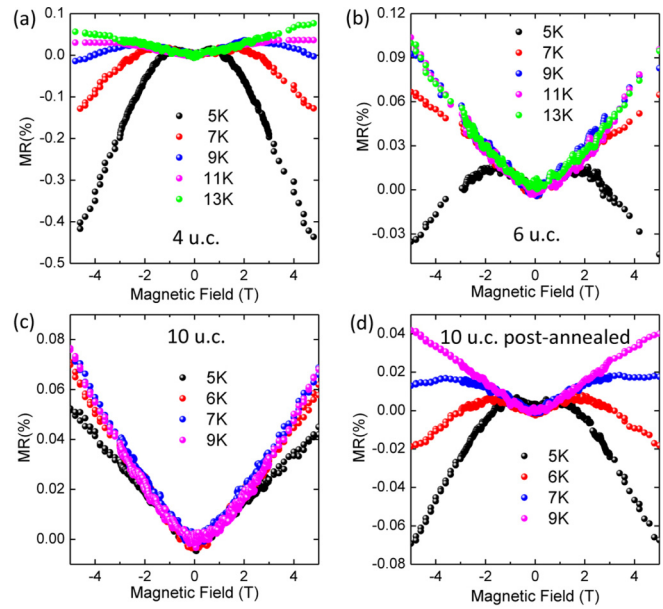

FIG. 7. Magnetoresistance (MR) in magnetic field perpendicular to the SVO films at different temperature and with the thickness of (a) 4-, (b) 6-, and (c) 10-u.c. as-grown films, compared with (d) 10-u.c. film postannealed in high vacuum under 850 °C for 40 min.

IV. CONCLUSION

We have grown SVO films in a layer-by-layer fashion and show the thickness-dependent metal-insulator transition with a critical thickness of ∼3 u.c. by UPS and STS. The structural, compositional, and oxidation state evolutions near the SVO/STO interface were studied by atomic-resolved HAADF STEM and STEM EELS. The reduction of the V oxidation state within the first 3 u.c. of SVO from the interface was observed. Combining it with Sr depletion within the same region, we conclude that significant oxygen deficiency occurs within the first 3 u.c. of SVO. From the transport and MR measurements of the SVO films with and without vacuum postannealing, we have confirmed that disorder-induced localization is the main driving force for the MIT in the SVO thin films, although we cannot rule out the importance of electron correlations.

ACKNOWLEDGMENTS

This work was primarily supported by U.S. DOE under Grant No. DOE DE-SC0002136. G.W. was supported by U.S. NSF under Grant No. DMR 1608865. The electronic microscopic work done at Brookhaven National Laboratory was sponsored by the U.S. DOE Basic Energy Sciences, Materials Sciences and Engineering Division under Contract No. DE-AC02-98CH10886.

[1] J. Orenstein and A. J. Millis, Science **288**, 468 (2000).
[2] *Colossal Magnetoresistive Oxides*, edited by Y. Tokura (Gordon and Breach, London, 2000).
[3] K. F. Wang, J. -M. Liu, and Z. F. Ren, Adv. Phys. **58**, 321 (2009).
[4] J. A. Moyer, C. Eaton, and R. Engel-Herbert, Adv. Mater. **25**, 3578 (2013).
[5] L. Zhang, Y. Zhou, L. Guo, W. Zhao, A. Barnes, H.-T. Zhang, C. Eaton, Y. Zheng, M. Brahlek, H. F. Haneef, N. J. Podraza, M. H. W. Chan, V. Gopalan, K. M. Rabe, and R. Engel-Herbert, Nat. Mater. **15**, 204 (2016).
[6] K. Yoshimatsu, T. Okabe, H. Kumigashira, S. Okamoto, S. Aizaki, A. Fujimori, and M. Oshima, Phys. Rev. Lett. **104**, 147601 (2010).
[7] K. Yoshimatsu, K. Horiba, H. Kumigashira, T. Yoshida, A. Fujimori, and M. Oshima, Science **333**, 319 (2010).
[8] J. Hubbard, Proc. R. Soc. London, Ser. A **276**, 238 (1963).
[9] Z. Zhong, M. Wallerberger, J. M. Tomczak, C. Taranto, N. Parragh, A. Toschi, G. Sangiovanni, and K. Held, Phys. Rev. Lett. **114**, 246401 (2015).
[10] Y. Okada, S.-Y. Shiau, T.-R. Chang, G. Chang, M Kobayashi, R. Shimizu, H.-T. Jeng, S Shiraki, H. Kumigashira, A. Bansil, H. Lin, and T. Hitosugi, Phys. Rev. Lett. **119**, 086801 (2017).
[11] H. Oka, Y. Okada, T. Hitosugi, and T. Fukumura, Appl. Phys. Lett. **113**, 171601 (2018).
[12] M. Chi, T. Mizoguchi, L. W. Martin, J. P. Bradley, H. Ikeno, R. Ramesh, I. Tanaka, and N. Browning, J. Appl. Phys. **110**, 046104 (2011).
[13] E. Abrahams, P. W. Anderson, D. C. Licciardello, and T. V. Ramakrishnan, Phys. Rev. Lett. **42**, 673 (1979).
[14] B. Kramer and A. MacKinnon, Rep. Prog. Phys. **56**, 1469 (1993).
[15] U. Aschauer, R. Pfenninger, S. M. Selbach, T. Grande, and N. A. Spaldin, Phys. Rev. B **88**, 054111 (2013).
[16] See Supplemental Material at http://link.aps.org/supplemental/10.1103/PhysRevB.100.155114 for details on the quantitative analysis of STEM images.
[17] C. J. Chen, *Introduction to Scanning Tunneling Microscopy* (Oxford University Press, New York, 1993).
[18] S. J. Pennycook and P. D. Nellist, *Scanning Transmission Electron Microscopy* (Springer, New York, 2011).
[19] Stuart B. Adler, J. Am. Ceram. Soc. **84**, 2117 (2001).
[20] A. Kalabukhov, R. Gunnarsson, J. Börjesson, E. Olsson, T. Claeson, and D. Winkler, Phys. Rev. B **75**, 121404(R) (2007).
[21] S. Miyoshi, J. -O. Hong, K. Yashiro, A. Kaimai, Y. Nigara, K. Kawamara, and J. Mizusaki, Solid State Ionics **161**, 209 (2003).
[22] Y. M. Kim, J. He, M. D. Biegalski, H. Ambaye, V. Lauter, H. M. Christen, S. T. Pantelides, S. J. Pennycook, S. V. Kalinin, and A. Y. Borisevich, Nat. Mater. **11**, 888 (2012).
[23] Q. Qiao, R. F. Klie, S. Öğüt, and J. C. Idrobo, Phys. Rev. B **85**, 165406 (2012).
[24] N. F. Mott and E. A. Davis, *Electronic Processes in Non-Crystalline Materials*, 2nd ed. (Clarendon, Oxford, 1979).
[25] L. Li, Z. Liao, Z. Diao, R. Jin, E. W. Plummer, J Guo, and J. Zhang, Phys. Rev. Mater. **1**, 034405 (2017).
[26] X. Shen, X. Qiu, D. Su, S. Zhou, A. Li, and D. Wu, J. Appl. Phys. **117**, 015307 (2018).
[27] R. Scherwitzl, S. Gariglio, M. Gabay, P. Zubko, M. Gibert, and J.-M. Triscone, Phys. Rev. Lett. **106**, 246403 (2011).
[28] B. L. Altshuler, D. Khmel'nitzkii, A. I. Larkin, and P. A. Lee, Phys. Rev. B **22**, 5142 (1980).
[29] G. Bergmann, Phys. Rep. **107**, 1 (1984).
[30] P. A. Lee and T. V. Ramakrishnan, Rev. Mod. Phys. **57**, 287 (1985).
[31] B. L. Altshuler, A. G. Aronov, and P. A. Lee, Phys. Rev. Lett. **44**, 1288 (1980).